



Nanoscale

**Confinement Induces Stable Calcium Carbonate Formation
in Silica Nanopores**

Journal:	<i>Nanoscale</i>
Manuscript ID	NR-ART-04-2022-001834.R1
Article Type:	Paper
Date Submitted by the Author:	08-Jun-2022
Complete List of Authors:	Asgar, Hassnain; Cornell University, School of Civil and Environmental Engineering Mohammed, Sohaib; Cornell University, Civil and Environmental Engineering Gadikota, Greeshma; Cornell University,

SCHOLARONE™
Manuscripts

Confinement Induces Stable Calcium Carbonate Formation in Silica Nanopores

Hassnain Asgar,^{1,‡} Sohaib Mohammed,^{1,‡} and Greeshma Gadikota^{1,*}

[‡]equal contribution

¹School of Civil and Environmental Engineering, Cornell University, Ithaca, NY 14853

* Corresponding Author. Phone: +1 607-255-4796. E-mail: gg464@cornell.edu

Abstract

Scalable efforts to remove anthropogenic CO₂ via the formation of durable carbonates require us to harness siliceous nanoporous geologic materials for carbon storage. While calcium carbonate formation has been extensively reported in bulk fluids, there is a limited understanding of the influence of nanoconfined fluids on the formation of specific stable and metastable polymorphs of calcium carbonates in siliceous materials that are abundant in subsurface environments. To address this challenge, silica nanochannels with diameters of 3.7 nm are architected and the formation of specific calcium carbonate phases is investigated using X-ray diffraction, scanning electron microscopy and molecular dynamics simulations. The formation of stable calcium carbonate (or calcite) is noted in silica nanochannels. The presence of fewer water molecules in the first hydration shell of calcium ions in confinement compared to in bulk fluids contributes to stable calcium carbonate formation. These studies show that nanoporous siliceous environments favor the formation of stable calcium carbonate formation.

Keywords: calcite, silica nanochannels; crystallization; MD simulations;

1 **1. Introduction**

2 Carbonate transformations regulate carbon cycling and maintain the earth's ecological
3 balance. Rising anthropogenic CO₂ concentrations in the air contribute to increasing global
4 temperatures¹ due to the greenhouse effect² and threaten our ecological balance.³ Achieving
5 tunable controls on carbon transformations is crucial for developing engineered processes for
6 decarbonization and achieving net negative carbon emission goals.^{4,5} Several approaches have
7 been proposed to capture and convert anthropogenic CO₂ emissions.^{6,7} Among these approaches,
8 carbon mineralization which involves converting CO₂ into solid inorganic carbonates⁸ is
9 thermodynamically downhill and can be engineered to store several gigatons of CO₂.^{9,10} Carbon
10 mineralization can be realized through the direct chemical interactions of solid calcium and
11 magnesium-bearing alkaline solid or aqueous resources with gaseous CO₂ or by dissolving CO₂ in
12 water to produce (bi)carbonate-rich fluids that react to produce solid calcium and magnesium
13 carbonates.^{11,12} The accelerated conversion of mobile CO₂ into solid carbonates in subsurface
14 geologic environments ensures permanent and safe storage and limits the need to monitor the fate
15 of CO₂ over several years. Similarly, engineered removal of CO₂ from air and water to produce
16 solid carbonates is a durable and quantifiable carbon management approach.

17 Despite the gigaton-scale potential for storing CO₂ in reactive subsurface formations such
18 as basalt¹³ and olivine,¹⁴ estimating the time scales of carbon mineralization is a challenge due to
19 anomalous carbon mineralization behavior in nanoconfinement.^{15,16} Pore sizes in ultramafic
20 minerals and rocks such as olivine and basalt can be smaller than 20 nm.¹⁷ In these nanoporous
21 environments, the interfacial organization of pore fluids contributes to anomalous carbonate
22 crystallization behavior that differs significantly from that of bulk fluids.

1 Achieving predictive control over the formation of calcium or magnesium carbonates in
2 confinement is crucial for several reasons. First, this approach enables the reconciliation of faster
3 than expected carbon mineralization rates in subsurface environments as opposed to predicted rates
4 as noted in the CarbFix project.¹³ Second, resolving the influence of interfacial water on the
5 formation of metastable or stable carbonate phases is crucial for developing engineered strategies
6 for carbon removal using porous materials. Third, the role of confinement in directing the
7 formation of specific carbonate phases preferentially assists with determining the associated
8 impact on storing gigaton levels of CO₂ in these environments. The formation of stable carbonates
9 such as calcite (CaCO₃) or magnesite (MgCO₃) is preferred since the structures of stable carbonate
10 remain unchanged over a long period and stoichiometric utilization of Ca²⁺ or Mg²⁺ ions to produce
11 stable carbonates is achieved. Stable carbonate phases have lower solubility compared to
12 metastable phases.^{18,19} Metastable carbonates, in contrast, gradually transform into stable
13 carbonates over time.²⁰ Examples of metastable calcium carbonate phases include spherical
14 vaterite (CaCO₃) and rosette-shaped aragonite (CaCO₃).^{21,22} Examples of metastable magnesium
15 carbonates include needle-like nesquehonite (MgCO₃·3H₂O),²³ sheet-like hydromagnesite
16 ((MgCO₃)₃(Mg(OH)₂)₂·4H₂O),²⁴ and platy lansfordite (MgCO₃·5H₂O).²³ The formation of
17 magnesium hydroxide in hydromagnesite is a less effective use of magnesium as opposed to the
18 complete utilization of magnesium to produce magnesite.

19 The confinement-mediated behavior of carbonates formation has been studied in the
20 context of biomineralization^{20,25–27} to understand exoskeleton growth in invertebrates. However, a
21 mechanistic understanding of how carbonates form in subsurface abundant nano-porous (pore
22 sizes 2 – 50 nm) siliceous matter remains unresolved despite the rising interest in engineered
23 carbon transformations for a sustainable climate, energy, and environmental future. While prior

1 studies reported the formation and stabilization of amorphous calcium carbonate in micron-level
2 confinement,²⁸ the influence of nanoscale confinement on the preferential formation of stable or
3 metastable calcium carbonate phases has not been studied. Various carbonate crystallization
4 mechanisms have been proposed to describe nucleation and growth mechanisms in bulk fluids but
5 are applicable under limited conditions. Classical nucleation growth (CNG), which describes a
6 first-order transition occurring via (i) nucleation of a solid phase and (ii) subsequent spontaneous
7 growth,²⁹ and classical crystal growth theory (CGT), which suggests a layer-by-layer growth of
8 carbonates once a critical size is reached, are applicable in limited scenarios.^{30,31} Alternatively, the
9 Ostwald Rule of Stages, in which the formation of stable crystalline phases is mediated by
10 intermediate metastable carbonate states with lower free energy barriers to nucleation, explains
11 specific observations related to stable calcite formation.³² However, this theory does not explain
12 observations of the direct formation of stable carbonates.³³

13 Alternatively, for crystal sizes smaller than 100 nm, size-dependent variation in the
14 enthalpic contributions of the free energy and small variations in enthalpic differences (e.g., 1–10
15 kJ/mol) was proposed to explain the formation of metastable vaterite, aragonite, and then calcite.³⁴
16 It is hypothesized that metastable to stable carbonate changes occur via solid-state transformations
17 and dissolution-precipitation mechanisms. For example, the transformations of amorphous
18 calcium carbonate (ACC) to biominerals that occur in the absence of water are attributed to solid-
19 state transformations.³⁵ Alternatively, the dissolution of more soluble metastable phases to produce
20 more stable and less soluble phases has been proposed.³⁶ This phenomenon, which is based on the
21 differences in the solubility of phases, is analogous to “Ostwald Ripening,” which describes size-
22 dependent dissolution and reprecipitation behavior.

1 Other non-classical theories such as “oriented attachment” describe the spontaneous self-
2 assembly of nanocrystalline particles along crystallographic faces to aid particle-mediated growth
3 of 1D, 2D, and 3D crystals.^{26,37,38} It was also hypothesized that differences in the ordering of the
4 solvent at solid interfaces and around ions can create free energy minima where nanoparticles can
5 reside without aggregating before the formation of a meso-crystalline structure.³⁹ Despite these
6 mechanistic insights, the dual effects of surface interactions and nanoscale confinement on
7 carbonate formation in siliceous nanopores with sizes ranging from 2 nm to 50 nm remain
8 unresolved. Advancing predictive controls into the carbon mineralization behavior in silica
9 nanopores is crucial for estimating the time scales for converting mobile CO₂ into stable
10 carbonates. Conversion of mobile CO₂ into mineralized solids limits the need to track the fate of
11 fluidic CO₂ and eliminates the risk of CO₂ ex-solution and preferential partitioning into the
12 atmosphere.

13 In carbon mineralization for Ca- and Mg- silicate interfaces, the reactions proceed in two
14 steps: (i) release of Ca²⁺ or Mg²⁺ ions by the dissolution of silicate phases in acidic conditions, and
15 (ii) nucleation of solid carbonates at pH > 8.⁴⁰ Carbon mineralization occurs when the
16 concentrations of the dissolved cations and carbonate species reaches supersaturation. Limiting
17 conditions for carbon mineralization can include CO₂ solvation, the insufficient concentration of
18 dissolved Ca and Mg species, and solid carbonate precipitation. Prior work in bulk fluids has
19 shown that dissolved carbonate concentrations from anthropogenic CO₂ can be enhanced using
20 biomimetic catalysts such as carbonic anhydrase^{41,42} and solvents such as amines and amino acids
21 ^{43–45}. Sufficiently high concentrations of dissolved carbonate ions in fluids bearing calcium ions
22 favor calcium carbonate precipitation. In this work, the influence of nanoscale confinement and
23 silica interfaces on directing the formation of stable or metastable calcium carbonate phases is

1 investigated. The specific scientific questions that motivate this study are: (a) How do we architect
2 silica nanochannels with ordered geometry and porosity to investigate the influence of
3 confinement on carbon mineralization? (b) What are the preferred structural orientations of
4 calcium carbonate grown in nanoscale confined environments? (c) What is the influence of the
5 organization of ions in confinement and surface interactions on calcium carbonate formation in
6 nanoscale confinement?

7 To address these research questions, silica nanochannels with well-ordered vertically
8 aligned pores with sizes of 3.7 nm were synthesized within alumina membranes using a sol-gel
9 approach. Calcium carbonate formation in these nanopores is achieved by reacting solutions of 0.1
10 M calcium nitrate ($\text{Ca}(\text{NO}_3)_2$) and 0.1 M sodium bicarbonate (NaHCO_3). The influence of the
11 differences in the hydration structure of Ca^{2+} ions at the pore surface and in the center of the pore
12 on the formation of calcium carbonate phases are inferred from molecular dynamics simulations.
13 This approach of developing architected materials to investigate calcium carbonate formation in a
14 calibrated manner sheds insights into the role of silica interfaces, interfacial fluids, and hydration
15 structure of Ca^{2+} ions in confinement on the preferential formation of specific calcium carbonate
16 phases in confinement. **Figure 1** is a schematic representation of the research approach. These
17 studies are particularly relevant since silica-based minerals and rocks are abundant in subsurface
18 environments^{10,13} where CO_2 storage via carbon mineralization at the scale of several gigatons is
19 proposed.

20 **2. Materials and Methods**

21 **2.1 Synthesis of Silica Nanochannels**

22 Silica nanochannels (SNCs) with well-defined pore sizes within anodic alumina
23 membranes (AAMs) are synthesized using a sol-gel approach. AAMs (Cytiva Whatman™

1 Anodisc™) having a diameter of 25 mm and a thickness of 60 μm are used. Silica is hydrolyzed
2 from tetraethylorthosilicate (TEOS) in ethanol and hydrochloric acid (HCl), while
3 cetyltrimethylammonium bromide (CTAB) is used as the structure-directing agent. In a typical
4 synthesis method, 7.68 g of ethanol, 11.57 g of TEOS, and 1 mL of 2.8 mM HCl are mixed at 60
5 °C for 90 minutes under reflux to pre-hydrolyze the solution. In a separate beaker, 1.52 g of CTAB
6 is dissolved in 4 mL of 55 mM HCl, and 15 g of ethanol under stirring for 30 minutes at 200 rpm
7 using the magnetic stirrer. Both solutions are mixed for 15 minutes at 400 rpm. To synthesize
8 SNCs in AAMs (pore sizes in AAM ~ 200 nm, pore length ~ 60 μm), the empty membranes are
9 loaded on the aspiration setup (**Figure 2**), and 0.5 mL of mixture solution is added to the membrane
10 under applied aspiration. Once the solution is passed through the membrane, 0.5 mL is added again
11 and allowed to pass through the membrane. This step is repeated 5 times and the membranes are
12 removed from the setup and rinsed with ethanol to avoid any precipitation on the sides of the
13 membranes. Finally, the membranes are placed at room temperature and the reaction is allowed to
14 proceed for 24 hours, which governs the formation of SNCs inside the pores of AAMs. CTAB is
15 removed from the inside of SNCs by heating AAM-SNCs at 250°C for 4 hours in a benchtop
16 muffle furnace (Thermo Scientific Thermolyne FB1410 M, Asheville, NC). The temperature
17 corresponding to the decomposition of CTAB is estimated from the thermogravimetric analysis of
18 AAM-SNCs, where the major weight loss associated with the degradation of CTAB is noted ~250
19 °C (**Figure S1 (a)**).

20 The weight (%) changes in the samples of interest during thermal treatment are determined
21 up to 800 °C with a ramp rate of 5 °C/min in an N₂ environment (purged at 25 mL/min) using a
22 Thermogravimetric Analyzer (TGA) (TA Instruments, SDT650, New Castle, DE). The pore size
23 distribution and specific surface area of silica nanochannels in AAM (AAM-SNCs) are determined

1 using the nonlocal density functional theory (NLDFT, Quantochrome AutoSorb iQ Analyzer,
2 Boynton Beach, FL) using N₂ adsorption isotherm at 77 K. Before measuring the isotherms, the
3 sample is outgassed at 90 °C for 24 hours. The morphological changes during the synthesis of
4 silica nanochannels are imaged using a scanning electron microscope (Zeiss LEO 1550 FESEM)
5 and transmission electron microscope (FEI F20 TEM) at 200 kV.

6 **2.2 Formation of Calcium Carbonate in Confinement**

7 To investigate the formation of calcium carbonate (CaCO₃) phases in confinement, 0.1 M
8 Ca(NO₃)₂ and 0.1 M NaHCO₃ solutions are mixed in a molar ratio of 1:1 and added to silica
9 nanochannels (SNCs). The silica nanochannels are constructed in the pores of anodic alumina
10 membranes (AAMs). A solution comprising 0.1 M Ca(NO₃)₂ and 0.1 M NaHCO₃ was loaded into
11 the silica nanochannels using an aspiration setup (**Figure S2**). The loading of the solutions into the
12 silica nanochannels was repeated five times to ensure full penetration into SNCs. The outer
13 surfaces of the membranes are cleaned with DI water to prevent calcium carbonate formation
14 outside the silica nanochannels. The structural evolution of the calcium carbonate phases is
15 determined using an X-ray diffractometer (XRD) (Bruker D8 Advance ECO Powder
16 Diffractometer) with Cu K α radiation, the acceleration voltage of 40 kV, and current of 25 mA.
17 The XRD patterns are obtained in the range of $2\theta = 20^\circ - 80^\circ$ after 6, 18, and 30 hours of reaction
18 time.

19 **2.3 Investigation of ion hydration and transport behavior using molecular-scale** 20 **simulations**

21 The hypothesis that the anomalous formation of calcium carbonate phases in confinement
22 compared to bulk fluids emerges from interactions with the silica surfaces, hydration structure of
23 calcium ions, and organization of interfacial fluids is investigated using molecular dynamics

1 simulations. For comparison, simulations of dissolved calcium ions in bulk fluids are performed.
2 Briefly, 0.1 M CaCO₃ solutions are simulated as bulk fluids while confined in cylindrical silica
3 nanopores with pore diameters of 3.7 nm at 298 K and 1 bar. The simulation cell for investigating
4 the hydration structure of calcium ions in bulk fluids has dimensions of 6 nm × 6 nm × 6 nm in *x*,
5 *y*, and *z* directions, respectively. The confinement environment is composed of a cylindrical silica
6 pore with 1 g/cm³ of 0.1 M CaCO₃ solution. The pore (*dia.* 3.7 nm) is cleaved in an amorphous
7 silica matrix with dimensions of 10.69 nm × 6.42 nm × 6.42 nm in *x*, *y*, and *z* directions,
8 respectively. The simulation cells used for investigating the hydration structure of calcium ions in
9 bulk and confined configurations are shown in **Figure 3**. Periodic boundary conditions are applied
10 on bulk and confined configurations in all three dimensions. The silica surface and water molecules
11 are modeled using parameters from CLAYFF⁴⁶ and flexible SPC/E forcefields,⁴⁷ respectively. The
12 OPLS/AA forcefield is used to model Ca²⁺ and CO₃²⁻ ions.⁴⁸ **Table S1** summarizes the interatomic
13 potentials.

14 The bulk and confined configurations are optimized through energy minimization using
15 the “steepest descent” approach for 50,000 steps. NVT simulations are performed on the bulk and
16 confined solutions for 50 ns. The temperature is held constant at 298 K using a Nose-Hoover
17 thermostat with a relaxation time of 0.1 ps.^{49,50} The intermolecular interactions of the simulated
18 systems are calculated as the sum of the electrostatic contributions for all Coulomb interactions
19 between the partial atomic charges and a short-range van der Waals dispersive interactions, given
20 by the Lennard-Jones potential. The equation of motion is integrated using the leapfrog algorithm
21 with a time step of 1 fs. The short-range interactions are calculated within a cutoff of 1.4 nm, while
22 the long-range electrostatic interactions are treated using Particle Mesh Ewald (PME).⁵¹ The non-
23 bonded van der Waals and electrostatic interactions are modeled using 12-6 Lennard-Jones and

1 coulombic models, respectively. The bonded interactions are accounted for in bond stretching,
2 angles bending and dihedrals, except for silica matrix where only OH bond stretching is
3 considered. All the simulations are conducted using Groningen Machine for Chemical
4 Simulations (GROMACS 2018) simulation package.⁵²

5 **3. Results and Discussion**

6 **3.1. Synthesis of Silica Nanochannels (SNCs)**

7 Sol-gel synthesis approaches provide unprecedented tunable controls on the particle and
8 pore morphologies of architected siliceous materials.^{53,54} The concept of dissolving a surfactant
9 (e.g., CTAB) and introducing and condensing silica around surfactant templates to direct sol-gel
10 formation has opened opportunities to synthesize particle and pore morphologies with specific
11 shapes and sizes. For example, amorphous silica,⁵³ forsterite (Mg_2SiO_4),⁵⁴ and wollastonite
12 (CaSiO_3)⁵⁵ with ordered pores ranging from 2–20 nm can be architected based on advances in sol-
13 gel and hydrothermal syntheses. One of the less explored approaches involves creating silica
14 nanochannels in existing porous templates to develop predictive controls over carbon
15 mineralization in confinement. Architecting these materials to study carbon mineralization
16 pathways will unlock unprecedented controls into the mechanisms underlying carbonate formation
17 in nanoconfined environments. To address this challenge, architected silica nanochannels were
18 developed in alumina membranes (**Figure 2**). The absence of any crystallinity in Amorphous
19 Alumina Membranes (AAMs) (by Cytiva WhatmanTM AnodiscTM and procured from Fisher
20 Scientific) is evident from the XRD patterns in **Figure S3 (a)**. These commercially available
21 AAM materials have pore sizes of ~200 nm as evident from the SEM image in **Figure. S3 (b)**.

22 The changes in the weight % of as-synthesized SNCs in AAMs before and after CTAB
23 removal were determined using thermogravimetric analysis (TGA) are shown in **Figure S1 (a)**.

1 For comparison, the TGA curve of as-received AAM is also shown. The major weight loss for as-
2 prepared SNCs in AAMs is noted around 250 °C, corresponding to the removal of CTAB.⁵⁶⁻⁵⁹ The
3 SNCs formed inside the pores of AAMs were imaged by dissolving the amorphous alumina
4 components in 10 wt.% H₃PO₄ solution for 24 hours and recovering SNCs via centrifugation. The
5 SEM image of SNCs obtained from dissolving the surrounding anodic alumina constituents is
6 shown in **Figure 4 (a)**. The formation of SNCs along the length of the membrane is noted in this
7 image. The cylindrical orientation of SNCs is evident from the TEM image in **Figure 4 (b)**. The
8 outer diameter of the nanochannels formed inside the pores of AAMs is ~200 nm which is
9 comparable to the pore size in AAMs. The uniformity and consistent lengths of the silica
10 nanochannels throughout the membranes evident from the TEM and SEM images in **Figure 4**
11 show the complete filling of AAM pores with the sol-gel precursor leading to the formation of
12 morphologically and chemically uniform SNCs. The average pore size, pore volume, and specific
13 surface area of SNCs in AAMs are 3.77 nm, 0.11 cc/g, and 57.17 m²/g, respectively. These
14 parameters are determined using the NLDFT method with a cylindrical silica pores model at 77 K
15 for liquid N₂. The uniformity of pore size distributions of SNCs with a pore diameter of 3.7 nm is
16 evident in **Figure 4 (c)**. The pore sizes and surface areas of AAM and SNCs in AAM are reported
17 in **Table 1**.

18 **3.2 Formation of Calcium Carbonates in Silica Nanochannels (SNCs)**

19 The hypothesis that nanoscale confinement contributes to the oriented growth of calcium
20 carbonate is investigated by injecting a solution comprising a mixture of 0.1 M Ca(NO₃)₂ and 0.1
21 M NaHCO₃ solutions into silica nanochannels to grow calcium carbonate. The formation of
22 calcium carbonate in silica nanochannels is evident from thermogravimetric analyses. The weight
23 loss associated with the dissociation of calcium carbonate on heating is evident from **Figure S1**

1 **(b).** Calcium carbonate formation is determined by collecting X-Ray Diffraction (XRD) data at 6,
2 18, and 30 hours after loading the calcium nitrate and sodium bicarbonate solutions into silica
3 nanochannels. The XRD patterns (**Figure 5**) reveal the dominant growth of the (104) plane of
4 calcium carbonate followed by the (214) plane. In rhombohedral calcite, the typical dominant
5 planes are (104), (113), (018), and (116). In contrast, the dominant planes in orthorhombic
6 aragonite are (111), (021), (012), (112), and (221). In metastable vaterite with hexagonal crystal
7 habitat, the dominant planes are (100), (101), (102), and (110). Complete XRD patterns of these
8 polymorphs of calcium carbonate are shown in **Figure S4** for comparison. The prominent planes
9 that distinguish calcite, aragonite, and vaterite phases are (104), (111), and (101), corresponding
10 to the d-spacings of 3.03 Å, 3.39 Å, and 3.29 Å, respectively.^{60,61} These results suggest that calcite,
11 the most stable polymorph of calcium carbonate is the preferred phase for durable carbon storage.
12 In this context, it is essential to consider differences in the stabilities of various polymorphs of
13 calcium carbonate. Calcite is a stable anhydrous polymorph of CaCO₃ with very low solubility in
14 water and remains unaltered over geological timescales. In contrast, aragonite is a metastable
15 anhydrous CaCO₃, which is thermodynamically unstable at standard temperature and pressure
16 conditions, and is converted to calcite in the presence of water due to its higher solubility in
17 water.⁶² Vaterite is another metastable anhydrous polymorph of CaCO₃ and does not exist under
18 ambient conditions. Vaterite is transformed to aragonite or calcite upon interaction with water and
19 is relatively rare in geological settings.^{62,63} Atomistic simulations on the energetic stability of these
20 polymorphs of CaCO₃ reveal that the (104) calcite surface is the most stable, having the lowest
21 surface energy value of 0.51 J/m². In contrast, the carbonate terminated surface of aragonite has a
22 smaller surface energy of 0.83 J/m² for the (111) plane. The surface energy for the carbonate

1 terminated (101) plane in vaterite is 0.79 J/m^2 .⁶⁴ These results show that the energetically efficient
2 polymorph of CaCO_3 is calcite.

3 In our XRD results, the distinct formation of (104) planes and the absence of (111) and
4 (101) planes in this study are indicative of the formation of calcite in silica nanochannels (**Figure**
5 **5**). The preferential growth of calcite along the (104) plane is attributed to the lowest density of
6 surface broken bonds among the other calcite surfaces^{65,66} and surface energy,^{65,67,68} and an equal
7 number of positive and negative charges.⁶⁹ Further, the (104) plane follows a flat (F) character as
8 shown in **Figure 5 (c)**.⁷⁰ The (214) plane becomes statistically significant after reaction for 30
9 hours. The reflections from the (214) plane can emerge from the particle growing in the vicinity
10 of the nanochannel wall and appears to develop its characteristic “step-like” (S) nature as the
11 growth along with the dominant (104) plane proceeds. The schematic comparison of flat (F) and
12 “step-like” (S) profiles for (104) and (214) planes along [441] zone axis is shown in **Figure 5 (c)**.
13 The crystallite sizes of 1.3 nm, 1.8 nm, and 1.9 nm after 6 hours, 18 hours, and 30 hours,
14 respectively, indicate a sluggish growth after first 6 hours (**Figure 5 (b)**). The growth of the calcite
15 phases is slower between 18 hours and 30 hours likely due to pore size constraints⁶⁵. These
16 measurements show the preferential formation of stable calcite phases over metastable calcium
17 carbonates in nanoscale confinement several hours after loading the initial solution bearing
18 calcium and bicarbonate ions into the nanochannels.

19 The sizes of the calcium carbonate crystallites are estimated from the XRD data using the
20 Scherrer equation (shown in equation (i)).^{71,72} In equation (i), D represents the average crystallite
21 size, $K = 0.9$ is Scherrer constant, λ is the wavelength of X-ray source used ($\text{Cu K}\alpha = 0.154 \text{ nm}$),
22 2θ is Bragg angle, and $B(2\theta)$ is the Full Width at Half Maximum (FWHM). The units of θ and
23 $B(2\theta)$ are radians.

$$D = \frac{K \cdot \lambda}{B(2\theta) \cdot \cos \theta} \quad (i)$$

Based on this expression, the crystallite sizes of calcite are estimated to be 1.3 nm, 1.8 nm, and 1.9 nm after 6 hours, 18 hours, and 30 hours of reaction time, respectively (**Figure 5 (b)**). The growth of the calcite phases is slower between 18 hours and 30 hours likely due to spatial constraints of the pore size.⁶⁵ These measurements directly suggest the formation of stable calcite phases preferentially over metastable calcium carbonates in nanoscale confinement several hours after loading the initial solution bearing calcium and bicarbonate ions into the nanochannels. The preferential orientation planes of calcite are (104) and (214) planes (**Figure 5 (a)** and **5 (c)**).

Prior studies investigating the formation of calcium carbonate in confinement showed that in Track Etch (TE) – membrane polycarbonate with micrometer-sized pores⁷³ and fungal hyphae tubular cells, amorphous calcium carbonate (ACC) is formed initially.⁷⁴ The amorphous calcium carbonate eventually transforms into calcite and aragonite phases. In TE-membrane polycarbonate with pore diameters of 25 nm, 50 – 800 nm, and 1200 nm, respective aragonite, aragonite and calcite, and calcite are formed at room temperature.⁷⁵ The formation of calcite in cylindrical pores of TE-membranes reported by Lotte and co-workers⁷³ is consistent with the findings of this study. Moreover, pH has a significant impact on the formation of calcium carbonate polymorphs. For example, calcite-like ACC and vaterite-like ACC are obtained at pH ~ 8.75 and 9.8 or higher, respectively. Aragonite-like ACC is obtained in multi-component ionic environments including in the presence of Mg²⁺ ions.⁷⁶ The pH of the solution in the silica nanochannels is closer to 8.75, which aligns with the initial formation of calcite-like ACC structure before transforming into calcite. Fewer water molecules in the coordination environment of Ca²⁺ ions^{77–79} in confinement compared to bulk fluids contribute to the formation of stable calcium carbonate. Fewer carbonate

1 ions in the first coordination shell of Ca^{2+} ions favor stable calcite formation over metastable
2 aragonite.⁸⁰ Additional factors to consider in the context of selective calcium carbonate
3 polymorphs include confinement-induced ion transport, concentration profiles, and changes in the
4 probability of nucleation.²⁸ The influence of ion transport, cation hydration behavior, and
5 concentration profiles on the formation of specific calcium carbonate polymorphs are investigated
6 using molecular dynamics simulations and discussed in the section below.

7 **3.3 Influence of Ion Hydration and Transport on Calcium Carbonate Formation**

8 Fundamental mechanistic insights into the organization, hydration, and transport of ions in
9 confinement leading to calcium carbonate (CaCO_3) formation in silica nanopores are investigated
10 using MD simulations. Simulations are performed in bulk and in confined fluids to contrast ion
11 organization, hydration, and transport behavior leading to CaCO_3 formation in these environments.
12 The static structure of the pre-nucleated CaCO_3 solutions in bulk and confined fluids is described
13 by the radial distribution function ($g(r)$) (**Figure 6**) and the corresponding coordination number
14 ($n(r)$) (**Figure 7**) of water-oxygen (O_{water}) and carbonate-oxygen ($\text{O}_{\text{Carbonate}}$) atoms in the first
15 coordination shell of Ca^{2+} ions. $g(r)$ and $n(r)$ are averaged over the last 10 ns of the simulation
16 time to ensure equilibrated structure of water- and carbonate-oxygen in the first coordination shell
17 of Ca^{2+} ions. The number of water molecules in the first coordination shell of Ca^{2+} ions in bulk
18 environments is about 7.2, which is consistent with reported X-ray scattering measurements and
19 molecular simulation studies.⁸¹ It is interesting to note that a higher number of oxygen atoms
20 corresponding to CO_3^{2-} ions are evident in the first coordination shell of Ca^{2+} ions compared to
21 oxygen atoms corresponding to water molecules (**Figure 7 (a) and Table 2**). The number of
22 oxygen atoms corresponding to the carbonate ions in the first coordination shell of Ca^{2+} cations is
23 4.23 ± 0.03 (**Figure 7 (b) and Table 2**), which is in agreement with the findings of Wang and co-

1 workers after accounting for the difference in the solutions' concentrations.⁸² Confinement induces
2 significant changes in the hydration structure of Ca^{2+} ions such that it reduces the number of
3 oxygen atoms corresponding to the water molecules in the first coordination shell of the Ca^{2+} ion
4 compared to the bulk fluids. The number of oxygen atoms corresponding to the water molecules
5 in the nanopores decreased to $3.03 \pm 3 \times 10^{-2}$ and $2.55 \pm 5 \times 10^{-2}$ in the first coordination shells of
6 the Ca^{2+} ion in the pore center and at the pore surface, respectively (**see Table 2**). The dehydration
7 of Ca^{2+} ions in the nanopores is associated with the structural alterations of oxygen atoms
8 corresponding to the carbonate species in the first coordination shell of the Ca^{2+} ion. The number
9 of oxygen atoms corresponding to the carbonate species in the first coordination shell increases to
10 $4.51 \pm 1 \times 10^{-2}$ for the Ca^{2+} ion in the pore center while it decreased to $4.08 \pm 3 \times 10^{-2}$ for Ca^{2+} ions
11 at the pore surface (**see Table 2**). The dehydration of calcium carbonates, mainly by heating,
12 promotes the transformation of amorphous to crystalline morphologies such as the transformation
13 of amorphous calcium carbonate (ACC) to mesostructured calcite.⁷⁷⁻⁷⁹ Thus, fewer water
14 molecules in the coordination environment of Ca^{2+} ions in confined fluids provide another
15 dehydration pathway to tune the transformation of metastable amorphous carbonate structures to
16 crystalline calcite morphologies.

17 Confinement was also found to have a significant influence on the transport behavior of
18 ions. Significant differences are noted in the self-diffusion coefficients and the local distribution
19 of Ca^{2+} , CO_3^{2-} and water in bulk fluids and those confined in pores. In bulk fluids, the diffusion
20 coefficients of Ca^{2+} , CO_3^{2-} and water molecules are $(0.63 \pm 0.03) \times 10^{-5}$, $(0.63 \pm 0.02) \times 10^{-5}$ and
21 $(2.51 \pm 0.12) \times 10^{-5}$ cm^2/sec , respectively (**Table 3**). These values are consistent with the diffusion
22 coefficients reported by Wang and co-workers.⁸²

1 Significant differences in the diffusion coefficients of ions in bulk and confined fluids were
2 noted. The diffusivity of Ca^{2+} and CO_3^{2-} ions at the pore surface is more than two orders of
3 magnitude lower compared in the center of the pore due to surface diffusion. The nucleation and
4 growth of calcium carbonate crystals are directly related to the diffusion of calcium and carbonate
5 ions. Prior MD simulations and experiments showed that the nucleation rate of CaCO_3 crystals in
6 bulk solvents increases exponentially with the enhanced diffusion of ions.⁸³ The diffusion of Ca^{2+}
7 and CO_3^{2-} ions have been controlled by using various additives including other ions such as Na^+ ,
8 Cl^- and OH^- ,⁸⁴ glycerol,⁸³ and poly(acrylic acid) (PAA).⁸⁵ Reduced diffusivity of Ca^{2+} and CO_3^{2-}
9 ions observed on adding these additives to the aqueous solutions is attributed to the formation of
10 ion pairs between Ca^{2+} and CO_3^{2-} with the added ions, enhanced solution viscosity on adding
11 glycerol and controlled the directional diffusion of ions in hydrogels using PAA. Furthermore, the
12 morphology of the formed carbonate crystals can be tuned by controlling ion diffusion. In addition
13 to the nucleation enhancement, slowing the diffusion of ions enables tuning the morphology of the
14 formed carbonate crystals. In this context, Wang and co-workers⁸⁶ showed that a decrease in the
15 diffusion of calcium and carbonate ions promotes the formation of vaterite and aragonite crystals
16 and the joint effect of the diffusion-reaction leads to the formation of cubic and needle-like
17 particles. Similarly, Jo and co-workers⁸⁷ found that the gradual decrease in the diffusion of ions
18 results in morphological transitions from hopper-like to rosette-like and otoconia-like calcite
19 structures. Kim and co-workers demonstrated that controlling the diffusion of the ions by adding
20 poly(acrylic acid) in hydrogel results in a variety of calcite morphologies including elliptical and
21 spherical calcite structures.⁸⁵ These studies support our finding that significantly reduced
22 diffusivities of ions at the pore surface contributes to the formation of stable calcite phases.

1 **4. Conclusions**

2 Understanding the pathways of carbon mineralization in subsurface-related, silica-rich
3 reservoirs is essential to meet the future goals of energy landscape. In this context, the
4 mineralization mechanisms in reservoirs with nanoscale confinements needs investigation due to
5 their abundance at the proposed mineralization sites. In this work, we study the nucleation of
6 calcium carbonate in silica nanochannels having diameter = 3.7 nm and report the preferential
7 formation of stable calcite phase over metastable aragonite or vaterite phases. From molecular
8 dynamics simulations, we note relatively fewer water molecules of hydration and a higher number
9 of carbonate ions surrounding calcium ion (Ca^{2+}) in confinement compared to bulk fluid. The
10 number of oxygen atoms around Ca^{2+} in confinement is 6, which is a suitable condition for calcite
11 formation compared to aragonite formation (9 oxygen atoms). The formation of stable carbonates
12 is favorable for the permanent storage of CO_2 , especially in silica-rich reservoirs.

13 **Acknowledgments**

14 The authors gratefully acknowledge the support of the College of Engineering at Cornell
15 University and the NSF CAREER award (# 2144373) for G. G. H. A.'s involvement is supported
16 by the DOE Energy Frontiers Research Center (EFRC) Multi-Scale Fluid-Solid Interactions in
17 Architected and Natural Materials (MUSE) funded by the U.S. Department of Energy, Office of
18 Science, Basic Energy Sciences under Award #DE-SC0019285. Electron microscopy imaging is
19 made possible through the Cornell Center for Materials Research (CCMR) #DMR-1719875
20 supported by the National Science Foundation Materials Research Science and Engineering
21 Centers (MRSEC) program (DMR 1120296).

References

- 1 J. F. B. Mitchell, *Rev. Geophys.*, 1989, **27**, 115–139.
- 2 J. S. Sawyer, *Nature*, 1972, **239**, 23–26.
- 3 A. D. McGuire, L. G. Anderson, T. R. Christensen, S. Dallimore, L. Guo, D. J. Hayes, M. Heimann, T. D. Lorenson, R. W. Macdonald and N. Roulet, *Ecol. Monogr.*, 2009, **79**, 523–555.
- 4 S. J. Davis, N. S. Lewis, M. Shaner, S. Aggarwal, D. Arent, I. L. Azevedo, S. M. Benson, T. Bradley, J. Brouwer, Y.-M. Chiang, C. T. M. Clack, A. Cohen, S. Doig, J. Edmonds, P. Fennell, C. B. Field, B. Hannegan, B. Hodge, M. I. Hoffert, E. Ingersoll, P. Jaramillo, K. S. Lackner, K. J. Mach, M. Mastrandrea, J. Ogden, P. F. Peterson, D. L. Sanchez, D. Sperling, J. Stagner, J. E. Trancik, C. Yang and K. Caldeira, *Science (80-.)*, 2018, **360**, 1–9.
- 5 R. S. Haszeldine, S. Flude, J. Gareth and V. Scott, *Phil. Trans. R. Soc. A*, 2018, **376**, 1–23.
- 6 P. J. A. Kenis, A. Dibenedetto and T. Zhang, *ChemPhysChem*, 2017, **18**, 3091–3093.
- 7 Z. Zhang, S. Pan, H. Li, J. Cai, A. Ghani, E. John and V. Manovic, *Renew. Sustain. Energy Rev.*, 2020, **125**, 109799.
- 8 G. Gadikota, *Nat. Rev. Chem.*, 2020, **4**, 78–89.
- 9 B. Sigf, C. Marieni, D. G. Sigur and E. H. Oelkers, *Nat. Rev. Earth Environ.*, 2020, **1**, 90–102.
- 10 B. P. Mcgrail, F. A. Spane, E. C. Sullivan, D. H. Bacon and G. Hund, *Energy Procedia*, 2011, **4**, 5653–5660.
- 11 G. Gadikota and A. hyung A. Park, *Accelerated Carbonation of Ca- and Mg-Bearing Minerals and Industrial Wastes Using CO₂*, Elsevier B.V., 2015.
- 12 E. Environ, A. Sanna, R. Hall and M. Maroto-valer, *Energy Environ. Sci.*, 2012, **5**, 7781–7796.
- 13 J. M. Matter, W. S. Broecker, M. Stute, S. R. Gislason, E. H. Oelkers, A. Stefánsson, D. Wolff-Boenisch, E. Gunnlaugsson, G. Axelsson and G. Björnsson, *Energy Procedia*, 2009, **1**, 3641–3646.
- 14 P. B. Kelemen and J. Matter, *Proc. Natl. Acad. Sci. U. S. A.*, 2008, **105**, 17295–17300.
- 15 Q. R. S. Miller, D. A. Dixon, S. D. Burton, E. D. Walter, D. W. Hoyt, A. S. Mcneill, J. D. Moon, K. S. Thanthiriwatte, E. S. Ilton, O. Qafoku, C. J. Thompson, H. T. Schaeff, K. M. Rosso and J. S. Loring, *J. Phys. Chem. C*, 2019, **123**, 12871–12885.
- 16 Q. R. S. Miller, M. E. Bowden, J. P. Kaszuba and H. T. Schaeff, *Chem Comm*, 2019, **55**, 6835–6837.
- 17 I. Rigopoulos, K. C. Petallidou, M. A. Vasiliades, A. Delimitis, I. Ioannou, A. M. Efstathiou and T. Kyratsi, *Powder Technol.*, 2015, **273**, 220–229.
- 18 M. Hänchen, V. Prigiobbe, R. Baciocchi and M. Mazzotti, *Chem. Eng. Sci.*, 2008, **63**, 1012–1028.
- 19 J. A. Kittrick and F. J. Peryea, *Soil Sci. Soc. Am. J.*, 1986, **50**, 243–247.
- 20 C. Rodríguez-Navarro, E. Ruiz-Agudo, J. Harris and S. E. Wolf, *J. Struct. Biol.*, 2016, **196**, 260–287.
- 21 S. Gopi, V. K. Subramanian and K. Palanisamy, *Mater. Res. Bull.*, 2013, **48**, 1906–1912.

- 22 J. K. Moore, J. A. Surface, A. Brenner, P. Skemer, M. S. Conradi and S. E. Hayes, *Environ. Sci. Technol.*, 2015, **49**, 657–664.
- 23 D. W. Ming and T. William, *Soil Sci. Soc. Am. J.*, 1985, **49**, 1303–1308.
- 24 C. M. Janet, B. Viswanathan, R. P. Viswanath and T. K. Varadarajan, *J. Phys. Chem. C*, 2007, **111**, 10267–10272.
- 25 A. M. Belcher, X. H. Wu, R. J. Christensen, P. K. Hansma, G. D. Stucky and D. E. Morsetll, *Nature*, 1996, **381**, 56–58.
- 26 F. C. Meldrum and H. Co, *Chem. Rev.*, 2008, **108**, 4332–4432.
- 27 S. Mann, D. D. Archibald, J. M. Didymus, T. Douglas, B. R. Heywood, F. C. Meldrum and N. J. Reeves, *Science (80-.)*, 1993, **261**, 1286–1292.
- 28 Y. Wang, M. Zeng, F. C. Meldrum and H. K. Christenson, *Cryst. Growth Des.*, 2017, **17**, 6787–6792.
- 29 J. W. Mullin, *Crystallization*, Oxford: Butterworth-Heinemann, Third., 1993.
- 30 W. K. Burton, N. Cabrera and F. C. Frank, *Philos. Trans. R. Soc. London. Ser. A, Math. Phys. Sci.*, 1951, **243**, 299–358.
- 31 J. J. De Yoreo, L. A. Zepeda-Ruiz, R. W. Friddle, S. R. Qiu, L. E. Wasylenki, A. A. Chernov, G. H. Gilmer and P. M. Dove, *Cryst. Growth Des.*, 2009, **9**, 5135–5144.
- 32 W. Ostwald, *Zeitschrift für Phys. Chemie*, 1897, **22**, 289–330.
- 33 C. Y. Tai and F. B. Chen, *AIChE J.*, 1998, **44**, 1790–1798.
- 34 A. Navrotsky, *Proc. Natl. Acad. Sci. Sci. United States Am.*, 2004, **101**, 12096–12101.
- 35 Y. U. T. Gong, C. E. Killian, I. C. Olson, N. P. Appathurai, A. L. Amasino, M. C. Martin, L. J. Holt, F. H. Wilt and P. U. P. A. Gilbert, *Proc. Natl. Acad. Sci. U. S. A.*, 2012, **109**, 6088–6093.
- 36 M. Schiro, E. Ruiz-Agudo and C. Rodríguez-Navarro, *Phys. Rev. Lett.*, 190AD, **26**, 265503.
- 37 R. L. Penn and J. F. Banfield, *Science (80-.)*, 1998, **281**, 969–971.
- 38 R. L. Penn and J. A. Soltis, *CrystEngComm*, 2014, **16**, 1409–1418.
- 39 R. Sathiyarayanan, M. Alimohammadi, Y. Zhou and K. A. Fichthorn, *J. Phys. Chem. C*, 2011, **115**, 18983–18990.
- 40 G. Gadikota and A. H. A. Park, *Accelerated Carbonation of Ca- and Mg-Bearing Minerals and Industrial Wastes Using CO₂*, 2014.
- 41 S. Zhang, Z. Zhang, Y. Lu, M. Rostam-Abadi and A. Jones, *Bioresour. Technol.*, 2011, **102**, 10194–10201.
- 42 T. N. Patel, A. H. A. Park and S. Banta, *Biotechnol. Bioeng.*, 2013, **110**, 1865–1873.
- 43 L. Ji, L. Zhang, X. Zheng, L. Feng, Q. He, Y. Wei and S. Yan, *J. CO₂ Util.*, 2021, **51**, 101653.
- 44 B. Yu, H. Yu, K. Li, L. Ji, Q. Yang, X. Wang, Z. Chen and M. Megharaj, *Environ. Sci. Technol.*, 2018, **52**, 13629–13637.
- 45 M. Liu, A. Hohenshil and G. Gadikota, *Energy and Fuels*, 2021, **35**, 8051–8068.

- 46 R. T. Cygan, J. J. Liang and A. G. Kalinichev, *J. Phys. Chem. B*, 2004, **108**, 1255–1266.
- 47 H. J. C. Berendsen, J. R. Grigera and T. P. Straatsma, *J. Phys. Chem.*, 1987, **91**, 6269–6271.
- 48 W. L. Jorgensen, D. S. Maxwell and J. Tirado-Rives, *J. Am. Chem. Soc.*, 1996, **118**, 11225–11236.
- 49 S. Nosé, *Mol. Phys.*, 1984, **52**, 255–268.
- 50 W. G. Hoover, *Phys. Rev. A*, 1985, **31**, 1695–1697.
- 51 T. Darden, D. York and L. Pedersen, *J. Chem. Phys.*, 1993, **98**, 10089–10092.
- 52 M. J. Abraham, T. Murtola, R. Schulz, S. Páll, J. C. Smith, B. Hess and E. Lindah, *SoftwareX*, 2015, **1–2**, 19–25.
- 53 S.-H. Wu, C.-Y. Mou and H.-P. Lin, *Chem. Soc. Rev.*, 2013, **42**, 3862–3875.
- 54 X. Gao, H. Asgar, I. Kuzmenko and G. Gadikota, *Microporous Mesoporous Mater.*, 2021, **327**, 111381.
- 55 J. Wei, F. Chen, J. Shin, H. Hong, C. Dai, J. Su and C. Liu, *Biomaterials*, 2009, **30**, 1080–1088.
- 56 S. A. Araujo, M. Ionashiro, V. J. Fernandes Jr and A. S. Araujo, *J. Therm. Anal. Calorim.*, 2001, **64**, 801–805.
- 57 R. Denoyel, M. T. J. Keene, P. L. Lllewellyn and J. Rouquerol, *J. Therm. Anal. Calorim.*, 1999, **56**, 261–266.
- 58 J. Goworek, A. Kierys, W. Gac, A. Borówka and R. Kusak, *J. Therm. Anal. Calorim.*, 2009, **96**, 375–382.
- 59 M. J. B. Souza, A. O. S. Silva, J. M. F. B. Aquino, V. J. Fernandes Jr and A. S. Araújo, *J. Therm. Anal. Calorim.*, 2004, **75**, 693–698.
- 60 C. G. Kontoyannis and N. V. Vagenas, *Analyst*, 2000, **125**, 251–255.
- 61 J. Chen and L. Xiang, *Powder Technol.*, 2009, **189**, 64–69.
- 62 M. M. H. Al Omari, I. S. Rashid, N. A. Qinna, A. M. Jaber and A. A. Badwan, in *Profiles of Drug Substances, Excipients and Related Methodology*, ed. H. G. B. T.-P. of D. S. Brittain Excipients and Related Methodology, Academic Press, 2016, vol. 41, pp. 31–132.
- 63 J. Wang and U. Becker, *Am. Mineral.*, 2009, **94**, 380–386.
- 64 W. Sekkal and A. Zaoui, *Sci. Rep.*, 2013, **3**, 1–10.
- 65 Z. Gao, C. Li, W. Sun and Y. Hu, *Colloids Surfaces A Physicochem. Eng. Asp.*, 2017, **520**, 53–61.
- 66 G. A. O. Zhi-yong, S. U. N. Wei, H. U. Yue-hua and L. I. U. Xiao-wen, *Trans. Nonferrous Met. Soc. China*, 2012, **22**, 1203–1208.
- 67 M. F. Roberto, B. Marco and A. Dino, *Cryst. Growth Des.*, 2010, **10**, 4096–4100.
- 68 M. Bruno, F. R. Massaro, M. Rubbo, M. Prencipe and D. Aquilano, *Cryst. Growth Des.*, 2010, **10**, 3102–3109.
- 69 D. Aquilano, F. Otálora, L. Pastero and J. M. García-ruiz, *Prog. Cryst. Growth Charact. Mater.*, 2016, **62**, 227–251.
- 70 D. Aquilano, M. Bruno, F. R. Massaro, M. Rubbo, V. V. Caluso and I.- Torino, *Cryst. Growth*

- Des.*, 2011, **11**, 3985–3993.
- 71 X. Gao, H. Asgar, I. Kuzmenko and G. Gadikota, *Microporous Mesoporous Mater.*, 2021, **327**, 111381.
- 72 H. P. Klug and L. E. Alexander, *X-ray Diffraction Procedures for Polycrystalline and Amorphous Materials*, Wiley, New York, 2nd edn., 1974.
- 73 E. Loste, R. J. Park, J. Warren and F. C. Meldrum, *Adv. Funct. Mater.*, 2004, **14**, 1211–1220.
- 74 A. Livne, S. C. Mijowska, I. Polishchuk, W. Mashikoane, A. Katsman and B. Pokroy, *J. Mater. Chem. B*, 2019, **7**, 5725–5731.
- 75 M. Zeng, Y. Y. Kim, C. Anduix-Canto, C. Frontera, D. Laundry, N. Kapur, H. K. Christenson and F. C. Meldrum, *Proc. Natl. Acad. Sci. U. S. A.*, 2018, **115**, 7670–7675.
- 76 A. Fernandez-Martinez, B. Kalkan, S. M. Clark and G. A. Waychunas, *Angew. Chemie - Int. Ed.*, 2013, **125**, 8512–8515.
- 77 C. Rodriguez-Navarro, K. Kudlacz, O. Cizer and E. Ruiz-Agudo, *Cryst. Res. Technol.*, 2015, **17**, 58–72.
- 78 J. D. Rodriguez-Blanco, S. Shaw and L. G. Benning, *Nanoscale*, 2011, **3**, 265–271.
- 79 A. V Radha, T. Z. Forbes, C. E. Killian, P. U. P. A. Gilbert and A. Navrotsky, *PNAS*, 2010, **107**, 16438–16443.
- 80 M. Saharay, A. O. Yazaydin and R. J. Kirkpatrick, *J. Phys. Chem. B*, 2013, **117**, 3328–3336.
- 81 D. Jiao, C. King, A. Grossfield, T. A. Darden and P. Ren, *J. Phys. Chem. B*, 2006, **110**, 18553–18559.
- 82 X. Wang, Y. Han, L. Lin, M. Fuji, T. Endo, H. Watanabe and M. Takahashi, *Model. Simul. Mater. Sci. Eng.*, , DOI:10.1088/0965-0393/16/3/035006.
- 83 X. Dou, H. Huang and Y. Han, *Chinese J. Chem. Eng.*
- 84 X. Wang, Y. Han, L. Lin, M. Fuji, T. Endo, H. Watanabe and M. Takahashi, *Model. Simul. Mater. Sci. Eng.*, , DOI:10.1088/0965-0393/16/3/035006.
- 85 H. L. Kim, Y. S. Shin and S. H. Yang, *CrystEngComm*, 2022, 42–44.
- 86 H. Wang, W. Huang and Y. Han, *Particuology*, 2013, **11**, 301–308.
- 87 M. K. Jo, Y. Oh, H. J. Kim, H. L. Kim and S. H. Yang, *Cryst. Growth Des.*, 2020, **20**, 560–567.

Tables

Table 1. Estimated pore sizes, pore volumes, and surface areas for anodic alumina membrane (AAM) and AAM containing silica nanochannels (AAM-SNC). The values are obtained from N₂ adsorption-desorption measurements using multi-point BET and non-local density functional theory models. Surface area from multi-point BET is obtained by fitting the first 7 points on the adsorption isotherm. Pore volume for AAM can not be estimated using the NLDFT or BJH method for AAM materials.

Sample ID	Pore Size (nm)	Pore Volume (cc/g)	Surface Area (m ² /g)
Anodic Alumina Membrane (AAM)	200 (SEM)	--	8.31 (Multi-point BET)
Silica Nanochannels (AAM-SNC)	3.7 (NLDFT)	0.11 (NLDFT)	71.65 (Multi-point BET)
			57.17 (NLDFT)

Table 2. The number of water oxygen (O_{Water}) and carbonate oxygens ($O_{\text{Carbonate}}$) in the first coordination shell of Ca^{2+} . Error bars represent the standard deviation from the mean values of three different simulations.

	Bulk Fluid	Away from Pore Surface	At Pore Surface
O_{Water}	$3.60 \pm 4 \times 10^{-2}$	$3.03 \pm 3 \times 10^{-2}$	$2.55 \pm 5 \times 10^{-2}$
$O_{\text{Carbonate}}$	$4.23 \pm 3 \times 10^{-2}$	$4.51 \pm 1 \times 10^{-2}$	$4.08 \pm 3 \times 10^{-2}$

Table 3. The self-diffusion coefficient (10^{-5} cm²/sec) of Ca²⁺, CO₃²⁻ and water in bulk and in confined systems. Error bars represent the standard deviation from the mean values of three different simulations.

	Bulk Fluid	Confinement	
		Away from Pore Surface	At Pore Surface
Ca²⁺	$63.0 \times 10^{-2} \pm 3 \times 10^{-2}$	$10.6 \times 10^{-2} \pm 4 \times 10^{-3}$	$0.24 \times 10^{-3} \pm 4 \times 10^{-5}$
CO₃²⁻	$62.8 \times 10^{-2} \pm 2 \times 10^{-2}$	$13.8 \times 10^{-2} \pm 6 \times 10^{-3}$	$4.92 \times 10^{-3} \pm 2 \times 10^{-4}$
Water	$251.0 \times 10^{-2} \pm 12 \times 10^{-2}$	$67.7 \times 10^{-2} \pm 9 \times 10^{-3}$	$21.10 \times 10^{-3} \pm 8 \times 10^{-4}$

Figure Captions

Figure 1. Schematic representation for (a) synthesis of silica nanochannels in alumina membranes, and (b) the formation of solid carbonates in silica nanochannels. (c) Radial distribution functions (RDFs) for Ca^{2+} - $\text{O}_{\text{carbonate}}$ species ‘at the pore surface’ and ‘pore center’ obtained from molecular dynamics simulations, and the corresponding snapshots of the simulations.

Figure 2. Schematic representation of steps involved in the synthesis of silica nanochannels (SNCs) inside the alumina membrane.

Figure 3. Snapshots of the initial configurations of (a) bulk and (b) confined CaCO_3 solutions in cylindrical silica nanopores with diameter of 3.7 nm. Calcium and carbonate atoms are shown in VDW drawing method while water and silica atoms are shown in Lines drawing method implemented in VMD software.

Figure 4. (a) Silica nanochannels (SNCs) formed inside the alumina membrane as viewed using Scanning Electron Microscopy (SEM) after dissolution of alumina membrane using 10 wt.% H_3PO_4 . (b) High resolution imaging of SNCs using Transmission Electron Microscope (TEM). (c) The pore size distribution of SNCs determined using N_2 adsorption-desorption measurements.

Figure 5. (a) Identification of stable calcite phases inside silica nanochannels (SNCs) acquired at different time intervals using X-ray Diffraction (XRD). (b) Crystallite sizes determined using Scherrer equation. (c) Schematic representation of calcite structure and growing (104) and (214) plane projected along the $[441]$ zone axis.⁷⁰

Figure 6. Radial distribution function $[g(r)]$ as a function of radius. (a) Calcium (Ca^{2+})-water oxygen (O_W) in bulk fluid. Inset: water in the first coordination shell of Ca^{2+} ion. (b) Ca^{2+} -carbonate oxygen (O_R) in bulk fluid. Inset: carbonate in the first coordination shell of Ca^{2+} ion. (c) Ca^{2+} - O_W in confinement (silica nanochannel). (d) Ca^{2+} - O_R in confinement. Insets in (c & d): Ca^{2+} and CO_3^{2-} ions in the pore center and at pore surface.

Figure 7. Coordination number $[n(r)]$ as a function of radius. (a) Calcium (Ca^{2+})-water oxygen (O_W) in bulk fluid. (b) Ca^{2+} -carbonate oxygen (O_R) in bulk fluid. (c) Ca^{2+} - O_W in confinement (silica nanochannel). (d) Ca^{2+} - O_R in confinement.

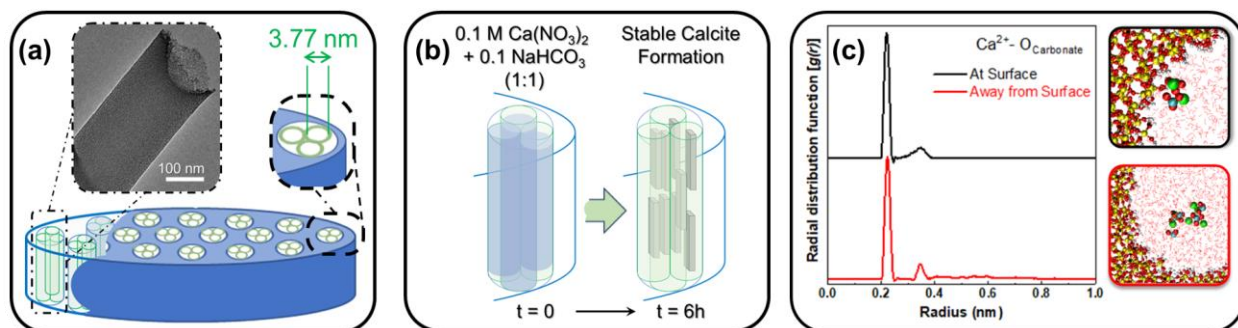


Figure 1. Schematic representation for (a) synthesis of silica nanochannels in alumina membranes, and (b) the formation of solid carbonates in silica nanochannels. (c) Radial distribution functions (RDFs) for Ca^{2+} - $\text{O}_{\text{carbonate}}$ species ‘at the pore surface’ and ‘pore center’ obtained from molecular dynamics simulations, and the corresponding snapshots of the simulations.

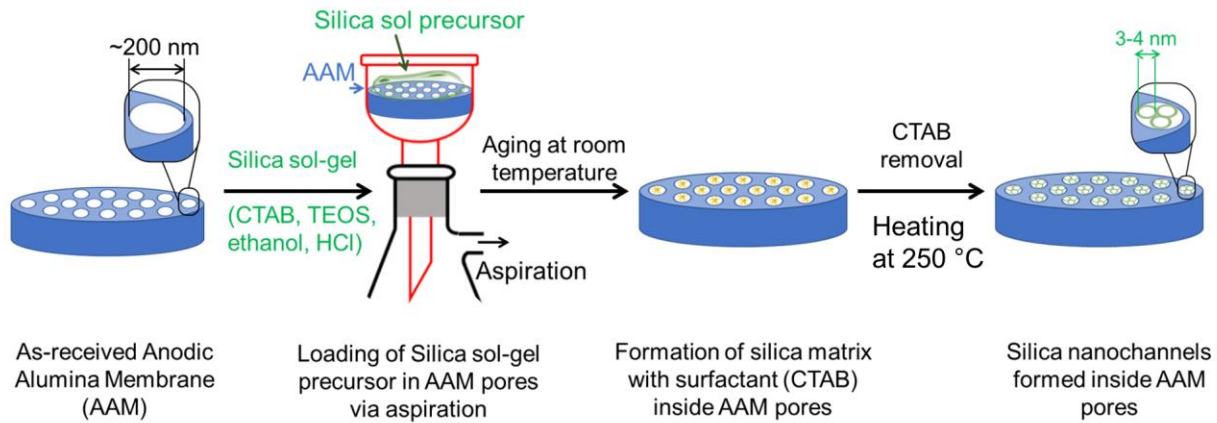


Figure 2. Schematic representation of steps involved in the synthesis of silica nanochannels (SNCs) inside the alumina membrane.

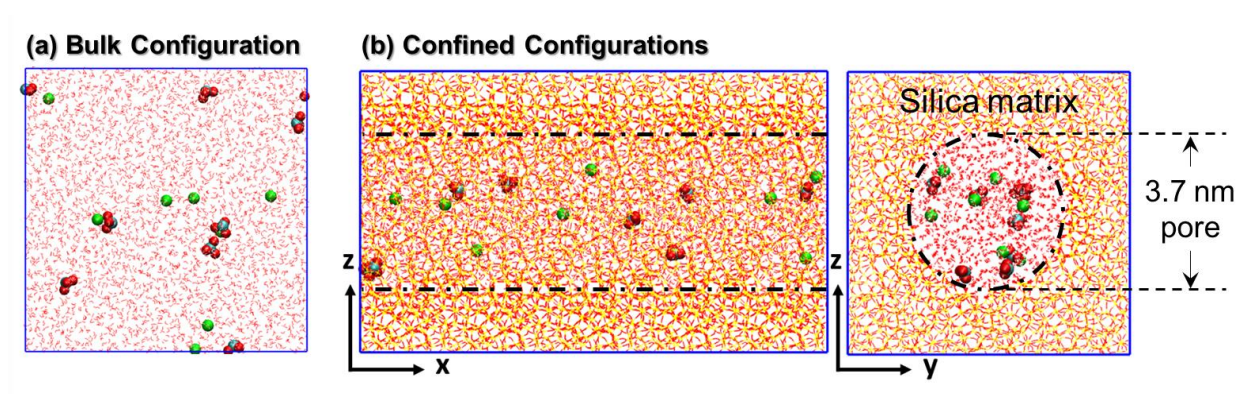


Figure 3. Snapshots of the initial configurations of **(a)** bulk and **(b)** confined CaCO_3 solutions in cylindrical silica nanopores with diameter of 3.7 nm. Calcium and carbonate atoms are shown in VDW drawing method while water and silica atoms are shown in Lines drawing method implemented in VMD software.

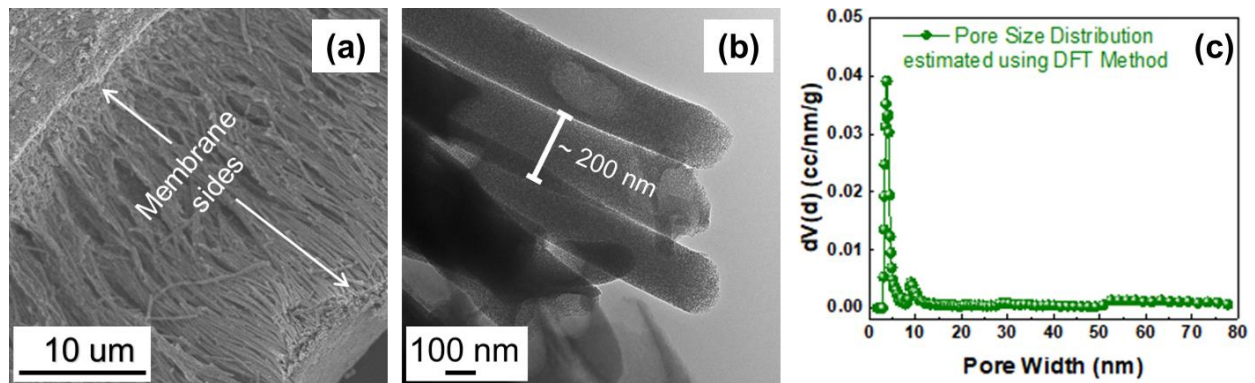


Figure 4. (a) Silica nanochannels (SNCs) formed inside the alumina membrane as viewed using Scanning Electron Microscopy (SEM) after dissolution of alumina membrane using 10 wt.% H_3PO_4 . (b) High resolution imaging of SNCs using Transmission Electron Microscope (TEM). (c) The pore size distribution of SNCs determined using N_2 adsorption-desorption measurements.

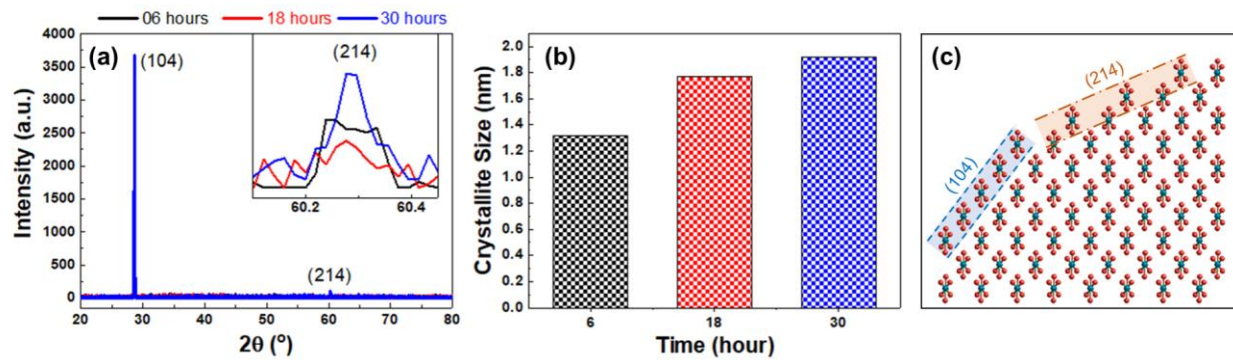


Figure 5. (a) Identification of stable calcite phases inside silica nanochannels (SNCs) acquired at different time intervals using X-ray Diffraction (XRD). (b) Crystallite sizes determined using Scherrer equation. (c) Schematic representation of calcite structure and growing (104) and (214) plane projected along the $[441]$ zone axis.⁷⁰

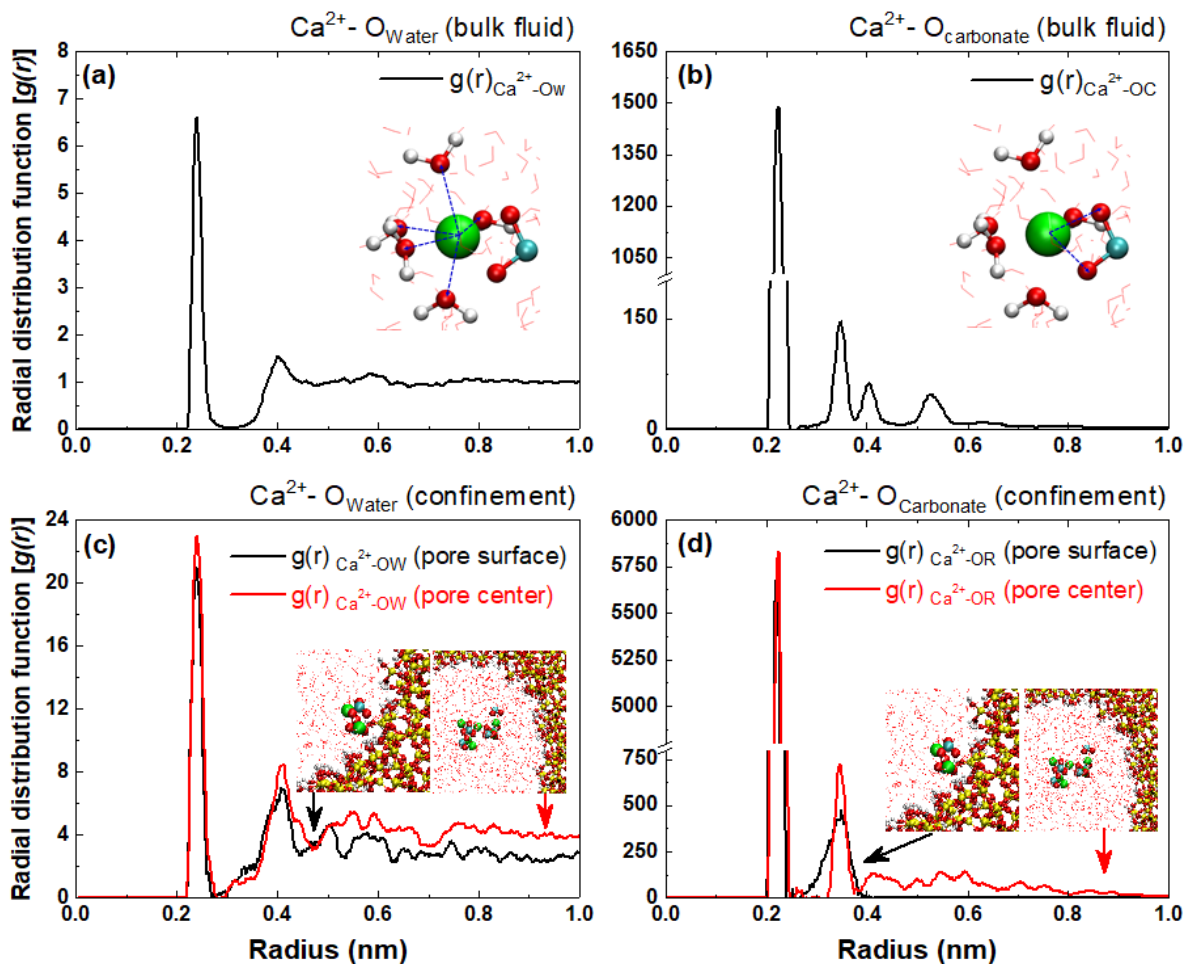


Figure 6. Radial distribution function $[g(r)]$ as a function of radius. **(a)** Calcium (Ca^{2+})-water oxygen (O_W) in bulk fluid. Inset: water in the first coordination shell of Ca^{2+} ion. **(b)** Ca^{2+} -carbonate oxygen (O_R) in bulk fluid. Inset: carbonate in the first coordination shell of Ca^{2+} ion. **(c)** Ca^{2+} - O_W in confinement (silica nanochannel). **(d)** Ca^{2+} - O_R in confinement. Insets in **(c & d)**: Ca^{2+} and CO_3^{2-} ions in the pore center and at pore surface.

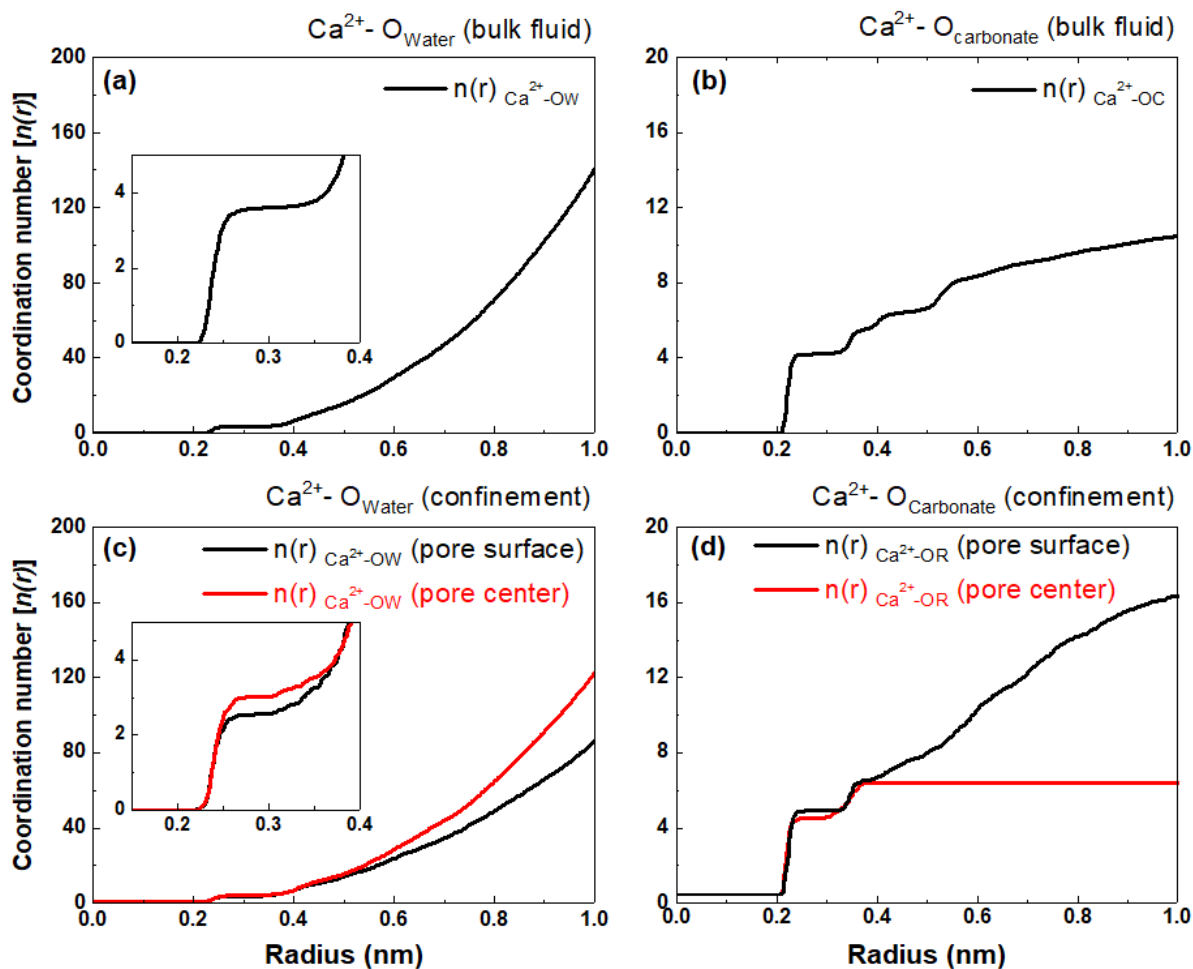


Figure 7. Coordination number $[n(r)]$ as a function of radius. (a) Calcium (Ca^{2+})-water oxygen (O_{w}) in bulk fluid. (b) Ca^{2+} -carbonate oxygen (O_{c}) in bulk fluid. (c) Ca^{2+} - O_{w} in confinement (silica nanochannel). (d) Ca^{2+} - O_{c} in confinement.